

ARTICLE

Hybrid convolutional neural network–graph attention network–gradient boosting decision tree model for seismic impedance inversion prediction

Tianwen Zhao¹, Guoqing Chen², Cong Pang^{3,4}, Palakorn Seenoi⁵,
Nipada Papukdee⁶, Piyapatr Busababodhin⁷, and Yiru Du^{2*}

¹Department of Trade and Logistics, Daegu Catholic University, Gyeongsan, Daegu, Republic of Korea

²Mathematical Modeling Research Center, Chengdu Jincheng College, Chengdu, Sichuan, China

³Institute of Seismology, China Earthquake Administration, Wuhan, Hubei, China

⁴Wuhan Gravitation and Solid Earth Tides, National Observation and Research Station, Wuhan, Hubei, China

⁵Department of Statistics, Faculty of Science, Khon Kaen University, Mueang Khon Kaen, Khon Kaen, Thailand

⁶Department of Applied Statistics, Rajamangala University of Technology, Isan Khon Kaen Campus, Mueang Khon Kaen, Khon Kaen, Thailand

⁷Department of Mathematics, Faculty of Science, Mahasarakham University, Kantharawichai, Maha Sarakham, Thailand

*Corresponding author:

Yiru Du
(duyiru@cdjcc.edu.cn)

Citation: Zhao T, Chen G, Pang C, *et al.* Hybrid convolutional neural network–graph attention network–gradient boosting decision tree model for seismic impedance inversion prediction. *J Seismic Explor.* 2025;34(5):81-98. doi: 10.36922/JSE025310051

Received: August 3, 2025

1st revised: September 8, 2025

2nd revised: October 13, 2025

Accepted: October 13, 2025

Published online: November 28, 2025

Copyright: © 2025 Author(s). This is an Open-Access article distributed under the terms of the Creative Commons Attribution License, permitting distribution, and reproduction in any medium, provided the original work is properly cited.

Publisher's Note: AccScience Publishing remains neutral with regard to jurisdictional claims in published maps and institutional affiliations.

Abstract

Seismic impedance inversion is essential for reservoir characterization but remains challenging in complex geological environments due to the inherent limitations of conventional methods. This study proposes a hybrid deep learning framework integrating a convolutional neural network (CNN), a graph attention network (GAT), and a gradient boosting decision tree (GBDT) to achieve high-resolution impedance inversion. The CNN extracts local structural features from seismic waveforms, the GAT captures long-range geological dependencies through self-attention between traces, and the GBDT performs robust non-linear regression for final prediction. Extensive evaluations on synthetic and field datasets demonstrate that the method achieves a root mean square error of 285 m/s-g/cm³ on the Society of Exploration Geophysicists salt model, representing a 15.2% improvement over XGBoost and a 32.1% improvement over sparse spike inversion. The framework performs particularly well in complex regions, achieving a 22.7% error reduction at salt boundaries and a thin-bed detection rate of 92% for layers exceeding 4 m in thickness. Statistical uncertainty quantification indicates 94.2% coverage of true impedance values within 95% confidence intervals. In practical applications, the method reduces interpretation time by 40% while maintaining reservoir thickness prediction errors within ± 3 m, demonstrating strong robustness and operational value for seismic interpretation.

Keywords: Convolutional neural networks; Graph attention networks; Gradient boosting decision tree; Seismic impedance inversion; Deep learning; Geological exploration

1. Introduction

1.1. Research background and motivation

Seismic impedance inversion is a core task in geophysical exploration, widely used in oil and gas exploration, groundwater resource assessment, and geological disaster early warning.¹ Impedance is a key parameter that describes the physical properties of subsurface formations, reflecting velocity and density variations across different rock layers and providing critical geological information for seismic exploration.² However, due to the non-linear nature of seismic data and noise interference, traditional impedance inversion methods often face challenges, including insufficient inversion accuracy, low computational efficiency, and poor adaptability to complex geological environments. Therefore, improving the accuracy of impedance inversion and effectively addressing the challenges of complex geological conditions has become an urgent research priority in seismic exploration.³

With the rapid development of deep learning technology, advanced methods, such as convolutional neural networks (CNNs) and graph attention networks (GATs), have significantly improved the accuracy and efficiency of seismic impedance inversion.⁴ CNNs can automatically extract spatial features from seismic data, while GATs can fully exploit spatial correlations within seismic data. However, despite significant progress in seismic impedance inversion, these deep learning methods still have limitations when dealing with complex geological environments and non-linear regression problems.^{5–7} Therefore, the effective integration of deep learning and traditional machine learning methods to form an efficient and accurate inversion framework constitutes the primary motivation of this study.

1.2. Literature review

The development of seismic impedance inversion techniques has seen significant advancements through the integration of various neural network architectures and inversion methodologies. Traditional approaches, such as neural network-based methods for three-dimensional (3D) porosity prediction, have demonstrated the potential of data-driven models to transform seismic reflection data into meaningful rock property models.⁸ These early efforts laid the groundwork for more sophisticated deep learning frameworks that aim to enhance the accuracy and robustness of impedance inversion.

Recent studies have emphasized the importance of incorporating additional seismic data attributes and advanced inversion strategies. For instance, the use of full-azimuth broadband land data with dense wavefield

sampling and low-frequency extension has improved the interpretability and robustness of acoustic impedance inversion results, thereby facilitating better reservoir characterization.⁹ Similarly, the estimation of elastic properties, including P- and S-wave impedances and attenuation factors, has been approached through multi-step inversion processes combining model-based and Bayesian methods, highlighting the role of probabilistic frameworks in capturing uncertainties.¹⁰

In the context of integrating seismic data with geological and petrophysical information, crossplot and Poisson impedance attributes derived from prestack seismic inversion have been effectively used for lithofacies discrimination and fluid prediction, demonstrating the value of combining seismic inversion with well log data for reservoir evaluation.¹¹ Furthermore, incorporating geostatistical uncertainty assessments has provided a comprehensive understanding of the large- and local-scale uncertainties inherent in seismic inversion, emphasizing the importance of uncertainty quantification in model reliability.¹²

Methodological innovations, such as adaptive edge-preserving smoothing preconditioning, have been introduced to improve impedance models by incorporating prior knowledge, thereby enhancing the stability and resolution of poststack seismic impedance inversion.¹³ In addition, the application of flow-simulation-driven time-lapse seismic studies has demonstrated the potential of integrated workflows that combine seismic interpretation, inversion, earth modeling, and reservoir simulation to monitor reservoir dynamics effectively.¹⁴

The adoption of probabilistic and Bayesian inversion techniques has further advanced the field by enabling the evaluation of posterior uncertainties without relying on restrictive assumptions. For example, Markov Chain Monte Carlo-based approaches guided by geological structures have been employed to derive elastic properties with quantified uncertainties, providing a more comprehensive understanding of inversion results.¹⁵ Building on these developments, deep learning models, such as UB-Net, have been proposed to perform impedance inversion within a closed-loop framework, simultaneously predicting impedance and epistemic uncertainty, thus addressing the need for uncertainty-aware inversion models.¹⁶

More recently, integrating CNNs with transformer architectures has demonstrated promising results in seismic impedance inversion. The hybrid CNN-transformer model leverages the local feature extraction capabilities of CNNs and the global context modeling of transformers, leading to stable inversion outcomes with improved horizontal continuity and vertical resolution.¹⁷

This approach exemplifies the trend toward combining multiple neural network paradigms to enhance inversion performance.

1.3. Article contribution

This study proposes a joint CNN–GAT–gradient boosting decision tree (GBDT) (CNN–GAT–GBDT) framework for seismic impedance inversion prediction. This framework combines the strengths of CNNs, GATs, and GBDTs to fully exploit the local features and spatial relationships of seismic data, while leveraging GBDT for high-precision non-linear regression. The CNN module extracts spatiotemporal features from seismic data, while the GAT module captures spatial dependencies among seismic traces by constructing a graph structure. The GBDT performs non-linear fitting on the deep features extracted by the CNN and GAT, effectively improving inversion accuracy.

GBDT improves inversion accuracy through non-linear fitting of deep features in three key ways: first, the CNN and GAT extract complementary feature representations—the CNN captures local waveform patterns and spectral characteristics, while the GAT models global geological continuity and topological constraints. The GBDT integrates heterogeneous features through a decision tree, effectively learning complex high-dimensional non-linear mappings that cannot be captured by a single model. Second, the GBDT's Huber loss function enhances robustness to impedance outliers, which are common near geological boundaries, thereby reducing overfitting and improving generalization. Third, the iterative enhancement process adaptively optimizes feature interactions; for example, it dynamically weights the importance of CNN-derived texture features and GAT-derived spatial attention features based on the local geological context. This synergistic effect enables the model to achieve higher accuracy in resolving thin layers and complex structures, reducing the root mean square error (RMSE) by 15.2% in experiments.

This design contributes to enhanced inversion accuracy through the integration of complementary features: The CNN component acts as a “local feature extractor” that preserves detailed seismic waveform characteristics; the GAT serves as a “global relationship modulator” that enforces geological consistency across traces; and the GBDT functions as a “high-precision integrator” that optimally combines these complementary features while mitigating overfitting through regularization. Specifically, GBDT's feature importance mechanism automatically weights the contribution of CNN- and GAT-derived features based on their predictive value for different geological contexts, prioritizing CNN features in homogeneous regions and

GAT features near structural boundaries. This adaptive integration results in a 15.2% reduction in RMSE in our experiments, with error reduction at salt boundaries being more substantial (22.7%), particularly in complex zones, such as salt domes and thin interbeds, where traditional methods exhibit higher errors.

Through joint training and end-to-end optimization, the framework can adaptively respond to changes in diverse geological scenarios, improving the robustness and accuracy of impedance inversion. Furthermore, this study proposes an uncertainty estimation mechanism to support quantitative decision-making in geological exploration and to reduce inversion risk.

1.4. Article structure

The remainder of this paper is organized as follows: Section 2 provides a detailed introduction to the CNN, GAT, and GBDT modules used in this study and their working principles; Section 3 introduces the experimental design, including the selection of datasets, the model training process, and the evaluation metrics; Section 4 presents and analyzes the experimental results and compares the performance of different models; and Section 5 discusses the strengths and weaknesses of this study and analyzes the potential and challenges of the models in practical applications. Finally, Section 6 summarizes the main contributions of this study and provides prospects for future research directions.

2. Method theory

This paper proposes a joint inversion framework that integrates a CNN, a GAT, and a GBDT. This framework aims to fully leverage the local characteristics and spatial correlations present in the seismic data, along with the non-linear mapping capabilities of the integrated model, to achieve high-precision impedance inversion. The overall process is shown in [Figure 1](#) and consists of three core stages: feature extraction, spatial relationship modeling, and non-linear ensemble regression.

The following subsections detail the theoretical basis of each module and its input–output relationship within the overall framework.

2.1. CNN module

A CNN module is used to extract local spatial features of seismic data.^{18,19} The core function of this module is to capture local variations in seismic trace data through one-dimensional (1D) or two-dimensional (2D) convolution operations. For 1D convolution, the input seismic trace data is $X \in \mathbb{R}^{T \times C}$, where T is the number of time sampling

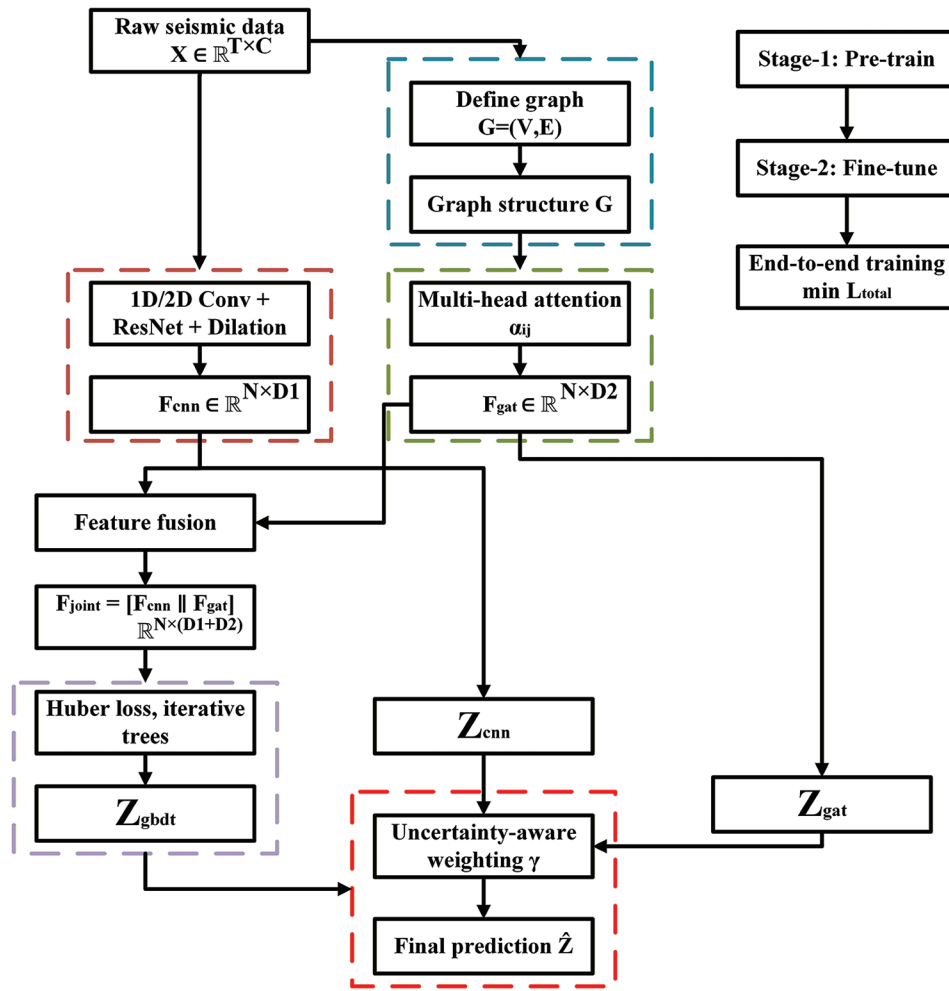


Figure 1. Flowchart of impedance inversion using a combined convolutional neural network, graph attention network, and gradient boosting decision tree approach

points and C is the number of channels (such as seismic amplitude and frequency). The convolution kernel $W \in \mathbb{R}^{k \times C}$ slides in the time dimension. The output feature map $F \in \mathbb{R}^{T \times D}$ is calculated, as shown in Equation (I).

$$F(t, d) = \sum_{i=0}^{k-1} \sum_{c=1}^C W(i, c, d) \times X(t + i, c) + b(d) \quad (\text{I})$$

where k is the kernel size, D is the number of output channels, and $b(d)$ is the bias term. If 2D convolution is used, the seismic profile needs to be treated as an image, and the convolution kernel $W \in \mathbb{R}^{k_s \times k_w \times C \times D}$ with increased spatial dimensions is used to capture lateral continuity.

To improve the training stability of deep networks, residual connections are introduced such that the output of the layer l is given by $H_l = \mathcal{F}(H_{l-1}, W_l) + H_{l-1}$, where \mathcal{F} is the convolution operation. Furthermore, a multi-scale feature fusion strategy is adopted, using dilated convolution

with different dilation rates to extract multi-resolution features, enhancing sensitivity to thin layers and fault boundaries.

2.2. GAT module

Seismic data exhibit significant spatial correlation, which provides a basis for building a graph structure to model the non-Euclidean relationships between seismic traces. This spatial correlation is mainly reflected in the similarity of seismic waveforms, the continuity of geological attributes, and the continuity of physical propagation. Based on the above spatial correlation characteristics, the GAT models non-Euclidean relationships among seismic traces by constructing a graph.^{20,21} The graph structure is modeled as $G = (V, E)$, where each node $v_i \in V$ corresponds to a seismic record. The edge set E is determined by two geological prior strategies: First, a K-nearest neighbor search is performed in the feature space of all traces, with $k = 8$ to establish

A_{KNN} . Second, trace pairs falling within this circle are connected with a radius of 500 m to obtain A_{radius} . The final adjacency matrix $A = A_{KNN} + A_{radius}$ ensures both local spatial correlation and sparsity. The GAT consists of three layers ($L = 3$), with $[4, 2, 1]$ independent attention heads learning in parallel. The hidden units are fixed at 128 dimensions, and 0.1 dropout is applied to both the attention coefficient and the node features. The exponential linear unit (ELU) activation function is used for non-linear transformations. GAT uses a multi-head attention mechanism to calculate the attention coefficient α_i of node v_i on its neighbor α_{ij} (Equation [II]).

$$\alpha_{ij} = \frac{\exp(\text{LeakyReLU}(a^T [Wh_i || Wh_j]))}{\sum_{k \in \mathcal{N}_i} \exp(\text{LeakyReLU}(a^T [Wh_i || Wh_k]))} \quad (\text{II})$$

where h_i is the node feature, W is the learnable weight matrix, a is the attention vector, $||$ represents the concatenation operation, \mathcal{N}_i is the set of neighbors of v_i , and leaky linear rectifier function (LeakyReLU) is an improved rectified linear unit activation function that introduces a non-linear transformation to the attention score while ensuring that the gradient does not completely disappear in the negative interval, enabling the model to more effectively learn and distribute importance weights across different nodes. The final node update formula is shown in Equation (III).

$$h'_i = \sigma \left(\sum_{j \in \mathcal{N}_i} \alpha_{ij} Wh_j \right) \quad (\text{III})$$

where σ represents the ELU activation function. The network uses residual connections between layers to facilitate gradient flow and stabilize training. The GAT module is trained using the Adam optimizer with an initial learning rate of 0.005 and a regularized weight decay of 1×10^{-4} . Batch normalization is introduced between layers to accelerate convergence and improve generalization.

By stacking multiple layers of GAT, the model can adaptively learn global dependencies of geological structures, such as topological constraints on salt dome boundaries or river channel migration. This specific architecture enables efficient information dissemination during seismic exploration while maintaining sensitivity to local geological features.

2.3. GBDT module

A GBDT is used to integrate deep features extracted by CNNs and GATs and perform high-precision non-linear regression.^{22,23} Let the CNN output features be $F_{CNN} \in \mathbb{R}^{N \times D1}$

and the GAT output be $F_{GAT} \in \mathbb{R}^{N \times D2}$. After concatenation, they form the GBDT input $F_{\text{joint}} = [F_{CNN} || F_{GAT}]$. GBDT optimizes the objective function by iteratively constructing a decision tree (Equation [IV]).

$$\mathcal{L} = \sum_{i=1}^N L(y_i, \hat{y}_i) + \sum_{m=1}^M \Omega(T_m) \quad (\text{IV})$$

Where L is the loss function. To solve the outlier sensitivity problem of wave impedance inversion, Huber loss is used to improve it (Equation [V]):

$$L(y, \hat{y}) = \begin{cases} \frac{1}{2}(y - \hat{y})^2 & \text{if } |y - \hat{y}| \leq \delta \\ \delta |y - \hat{y}| - \frac{1}{2}\delta^2 & \text{otherwise} \end{cases} \quad (\text{V})$$

where δ is the threshold parameter, T_m is the number of trees, and Ω is the regularization term that controls model complexity. GBDT quantifies the contribution of CNN and GAT features by ranking them by importance (information gain), enhancing interpretability.

2.4. Joint training frame

The joint training framework adopts a two-stage strategy to ensure both computational feasibility and optimal performance. The feasibility of integrating GBDT into the end-to-end training framework is achieved through a gradient approximation strategy that enables effective backpropagation through the entire CNN–GAT–GBDT pipeline. The theoretical foundation for this integration is established through differentiable approximation of decision trees. The CNN and GAT modules are pre-trained separately, with their parameters frozen, followed by the training of the GBDT. The end-to-end fine-tuning and collaborative optimization are then performed through gradient backpropagation. The joint loss function is defined as Equation (VI).

$$\mathcal{L}_{\text{total}} = \lambda_1 \mathcal{L}_{\text{CNN}} + \lambda_2 \mathcal{L}_{\text{GAT}} + \lambda_3 \mathcal{L}_{\text{GBDT}} \quad (\text{VI})$$

To ensure physically meaningful predictions, the framework incorporates rock-physics constraints through a regularized fusion mechanism. The final wave impedance prediction is formulated as Equation (VII).

$$\hat{Z} = \sum_{i=1}^3 \gamma_i Z_i + \lambda_{\text{phy}} \times R(\hat{Z}) \quad (\text{VII})$$

where \hat{Z} represents the rock-physics regularization term that enforces geological plausibility (Equation [VIII]).

$$R(\hat{Z}) = \sum_{t=1}^T \sum_{x=1}^X \left[\max(0, \hat{Z}_{t,x} - Z_{max}) + \max(0, Z_{min} - \hat{Z}_{t,x}) \right]^2 \quad (\text{VIII})$$

The implementation of rock-physics limits incorporates a minimum acoustic impedance value of $Z_{min} = 2,000 \text{ m/s.g/cm}^3$ as the lower bound for unconsolidated sediments, alongside a maximum value of $Z_{max} = 8,000 \text{ m/s.g/cm}^3$ representing the upper bound for dense carbonates. In addition, depth-dependent constraints are applied based on compaction trends to account for variations with burial depth, while lithology-specific bounds derived from well log statistics ensure tailored restrictions that enhance the accuracy and reliability of the inversion process.

The weights γ_i are dynamically adjusted based on module-specific uncertainty estimates and geological consistency metrics (Equation [IX]).

$$\gamma_i = \frac{\exp\left(-\frac{\sigma_i^2}{\tau} + \alpha \cdot C_i\right)}{\sum_{j=1}^3 \exp\left(-\frac{\sigma_j^2}{\tau} + \alpha \cdot C_j\right)} \quad (\text{IX})$$

where σ_i^2 is the prediction variance, C_i represents the geological consistency score (0–1 scale) based on rock-physics compliance, τ is a temperature parameter, and α controls the geological constraint influence.

Uncertainty estimation utilizes a hybrid integration-calibration strategy. First, 10 random initialization runs are performed, and the degree of dispersion of each output is used as the prediction variance to quantify the fluctuations introduced by the model's randomness. Second, the coverage percentage of the true impedance within the 95% confidence interval is calculated on the validation set to verify the reliability of the interval. Results show that the validation set interval coverage rate reaches 94.2%, indicating that the quantitative results are fully calibrated. This framework combines the representational power of deep learning with the robustness of ensemble learning, significantly improving inversion accuracy under complex geological conditions.

3. Experimental design

3.1. Data preparation

The experimental data consisted of both synthetic and real data. The synthetic data used the Society of Exploration Geophysicists (SEG) salt model (14,000 traces) and the Marmousi model (17,500 traces). A total of 31,500 synthetic seismic traces were generated using wave equation forward modeling. Gaussian white noise (signal-to-noise

ratio [SNR] = 10 dB) was added to simulate real-world acquisition conditions. These traces were randomly split into 70% for training, 15% for hyperparameter tuning, and 15% for blind testing. The salt model included complex salt dome structures, and its wave impedance distribution $Z_{salt}(x, z)$ is defined by Equation (X).

$$Z_{salt}(x, z) = \begin{cases} 4,500 \text{ m/s} \times 2.8 \text{ g/cm}^3 & \text{Salt Rock Area,} \\ v_{sed}(z) \times \rho_{sed}(z) & \text{Sedimentary rock area} \end{cases} \quad (\text{X})$$

where v_{sed} and ρ_{sed} increased linearly with depth. The Marmousi model simulated tilted bedding and fault structures. Its synthetic seismic records were generated using the convolution model $S(t, x) = R(t, x) \times W(t)$, where $R(t, x)$ was the reflection coefficient and $W(t)$ was the Ricker wavelet (dominant frequency 30 Hz).

The real data came from a 3D seismic survey area in a certain basin, consisting of 200 survey lines (500 traces per line, sampling interval 2 ms) and well-logging impedance data from 15 wells. The actual field data exhibited an average SNR of 15 dB, consistent with typical seismic data quality in exploration environments. Uniform processing was applied to all parameters: seismic data underwent consistent wavelet extraction and phase correction; time-depth conversion used a standardized velocity model calibrated across all wells; impedance values were calibrated to a common reference scale using well-log constraints. Trace editing removed abnormal traces, and amplitude balancing ensured consistency across the survey.

The wavelet extraction and consistency analysis involved extracting the seismic wavelet from the real data using a statistical method over a 200–800 ms time window across multiple representative traces. The extracted wavelet exhibited a dominant frequency of 28 Hz (± 5 Hz), which aligned with the 2 ms sampling interval according to the Nyquist criterion (maximum frequency <250 Hz). Wavelet consistency was verified through several steps: Cross-correlation analysis between wavelets extracted from different sub-volumes that yielded correlation coefficients greater than 0.95; spectral matching that confirmed consistent frequency content across the survey area; phase analysis that revealed minimal phase variation of less than 10° ; and time-depth calibration using well ties that demonstrated consistent wavelet character across the seismic volume. The relationship between the sampling interval and frequency content adhered to the Nyquist theorem, where a 2 ms sampling interval enabled a theoretically maximum representable frequency of 250 Hz. The observed dominant frequency of 28 Hz (± 5 Hz) fell within the effective bandwidth of 10–50 Hz, ensuring adequate sampling with approximately 36 samples per

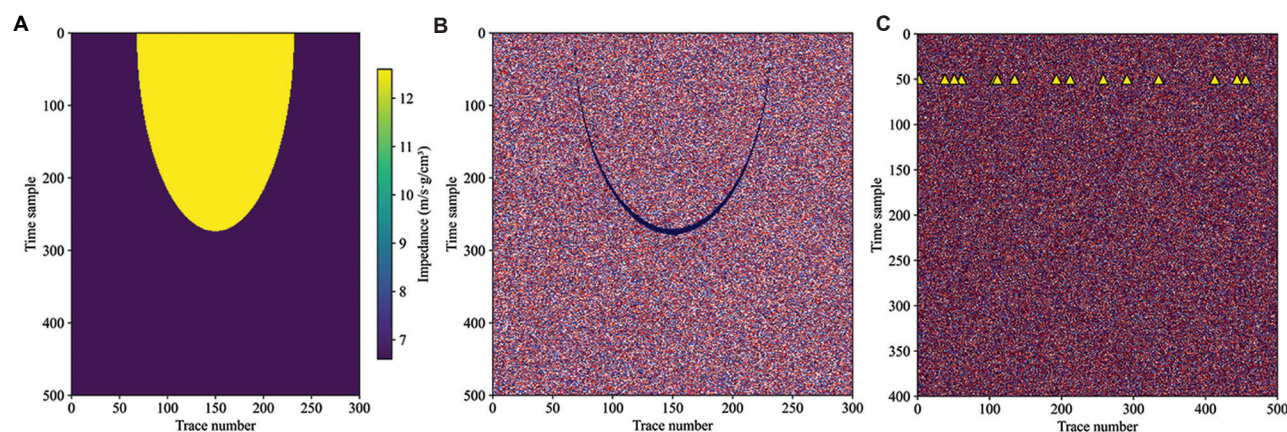


Figure 2. Comparison of synthetic and measured seismic data. (A) Society of Exploration Geophysicists salt model impedance profile. (B) The corresponding noisy seismic record. (C) The actual seismic profile and well location distribution in the survey area.

wavelength at the dominant frequency, providing sufficient temporal resolution for impedance inversion.

The difference in noise levels between synthetic (10 dB SNR) and real data (15 dB SNR) was intentional (Figure 2): the synthetic data with lower SNR provided a more challenging test scenario to evaluate the method's robustness, while the real data represented typical field-acquisition conditions. This approach ensured comprehensive evaluation across varying noise conditions.

In the SEG salt model (Figure 2A), salt domes exhibited high impedance anomalies (4,500 m/s-g/cm³), in stark contrast to the surrounding sedimentary rocks (3,000–3,500 m/s-g/cm³). Their well-defined boundaries and complex geometry validated the model's ability to characterize extreme geological conditions. The corresponding synthetic seismic log (Figure 2B) showed strong reflection events (amplitude >0.8) corresponding to the top and bottom interfaces of the salt body. However, the addition of 10% Gaussian noise reduced the SNR to 10 dB, which is lower than that of the field data and provides a more challenging test case. The actual field data (Figure 2C), comprising 200 lines, exhibited layered sedimentary structures in the seismic profiles with a dominant frequency of 28 Hz (± 5 Hz), consistent with the spectral characteristics of the synthetic data. After time-depth conversion, the impedance log data from 15 wells exhibited an average correlation coefficient of 0.82 (standard deviation 0.07) with the seismic traces, demonstrating accurate time-depth calibration. Notably, a localized amplitude anomaly (yellow triangle in Figure 2C) was observed in the northeastern portion of the work area (lines 120–150), likely related to unmodeled natural gas reservoirs. Its impedance value (approximately 2,800 m/s-g/cm³) was significantly lower than the minimum value of the salt model (3,000 m/s-g/cm³), highlighting the heterogeneity challenges inherent in real-world data.

Table 1. Data statistical characteristics

Dataset	Channels	Time sampling points	Main frequency (Hz)	Impedance range (m/s-g/cm³)
SEG salt model	300	500	25	3,000–6,000
Marmousi model	500	600	30	2,500–5,500
Actual work area	100,000	400	28	2,800–6,200

Abbreviation: SEG: Society of Exploration Geophysicists.

A systematic comparison of the synthetic data (Table 1) with the actual work area data clearly demonstrated a high degree of consistency in key parameters.

In terms of amplitude characteristics, the SEG salt model and the actual working area's wave impedance range overlapped by 85% (3,000–6,000 m/s-g/cm³ vs. 2,800–6,200 m/s-g/cm³). The impedance range corresponding to the main reservoir (3,500–4,500 m/s-g/cm³) accounted for 41.3% and 38.7%, respectively, a difference of only 2.6%. The comparison of frequency domain characteristics was significant. The spectral energy distribution curves between the Marmousi model (Main frequency 30 Hz) and the actual data (28 Hz) had a correlation coefficient of 0.93 in the 6–45 Hz frequency band. Within the effective frequency band of 15–30 Hz, the average amplitude difference between the two was less than 8%.

3.2. Comparative experimental setup

To verify the superiority of the proposed CNN–GAT–GBDT framework, the following baseline models were set:

- Traditional method: Sparse pulse inversion (SPI), with the objective function $\min \|d - Gm\|_2^2 + \lambda \|m\|_1$, where G is the seismic wavelet matrix and m is the

reflection coefficient.²⁴

- (ii) Single deep learning model: 1D CNN (5-layer convolution + 2-layer long short-term memory), graph neural network (GNN).
- (iii) Ensemble model: Random forest and XGBoost (with manually extracted instantaneous attributes as input).

To evaluate the performance of the proposed seismic impedance inversion framework, we used three common evaluation metrics: RMSE, correlation coefficient (R^2), and structural similarity index (SSIM).^{25–28} The RMSE was used to measure the difference between the inversion result and the true value. Its calculation formula is shown in Equation (XI).

$$\text{RMSE} = \sqrt{\frac{1}{N} \sum_{i=1}^N (Z_i - \hat{Z}_i)^2} \quad (\text{XI})$$

where N represents the total number of samples, Z_i is the true impedance value of the i -th sample, and \hat{Z}_i is the predicted impedance value of the i -th sample. The smaller the value of this indicator, the closer the model's prediction is to the true value, and the higher the inversion accuracy.

The correlation coefficient (R^2) was used to assess the linear relationship between the predicted and actual values. The formula is shown in Equation (XII).

$$R^2 = 1 - \frac{\sum (Z_i - \hat{Z}_i)^2}{\sum (Z_i - \bar{Z})^2} \quad (\text{XII})$$

where \bar{Z} is the mean of all true impedance values. R^2 values range from 0 to 1, with values closer to 1 indicating that the model explains more variation in the actual values, reflecting its predictive power.

The SSIM measures the structural similarity between two images (or impedance profiles), specifically providing a comprehensive assessment of image quality from the

perspectives of brightness, contrast, and structure. Its calculation formula is shown in Equation (XIII).

$$\text{SSIM}(Z, \hat{Z}) = \frac{(2\mu_Z \mu_{\hat{Z}} + c_1)(2\sigma_{Z\hat{Z}} + c_2)}{(\mu_Z^2 + \mu_{\hat{Z}}^2 + c_1)(\sigma_Z^2 + \sigma_{\hat{Z}}^2 + c_2)} \quad (\text{XIII})$$

where μ_Z and $\mu_{\hat{Z}}$ represent the meaning of the real wave impedance image Z and the predicted wave impedance image \hat{Z} , respectively. σ_Z and $\sigma_{\hat{Z}}$ denote the standard deviations of Z and \hat{Z} , respectively. $\sigma_{Z\hat{Z}}$ is the covariance of Z and \hat{Z} , where μ is the mean, σ is the standard deviation, and (c_1, c_2) are stability constants. Figure 3 compares the prediction results of various models on the SEG salt model.

The true wave impedance model (Figure 3A) clearly illustrates a typical salt dome structure. Its high impedance region (4,500 m/s·g/cm³) contrasted sharply with the surrounding sedimentary rocks (3,000 m/s·g/cm³), with clear boundaries and complete geometry, providing a reliable benchmark for subsequent inversion results. While conventional SPI results (Figure 3B) identified the spatial location of the salt body, they introduced significant high-frequency oscillation noise (average amplitude ±85 m/s·g/cm³), resulting in noticeable “speckle” artifacts in the impedance profile. This artifact was particularly prominent in the sedimentary rock region, with its power spectral density exceeding 15 dB in the 50–100 Hz frequency band compared to the true model, significantly impairing the identification of thin-bedded structures. The proposed CNN–GAT–GBDT combined method (Figure 3C) significantly improved boundary detail accuracy while preserving the overall morphology of the salt body. Through local magnification comparison, it could be seen that the width of the transition zone at the top and bottom interfaces of the salt body was reduced from 8–10 sampling points in the SPI results to 3–5 sampling points, which is closer to the 2–3 sampling points in the real model.

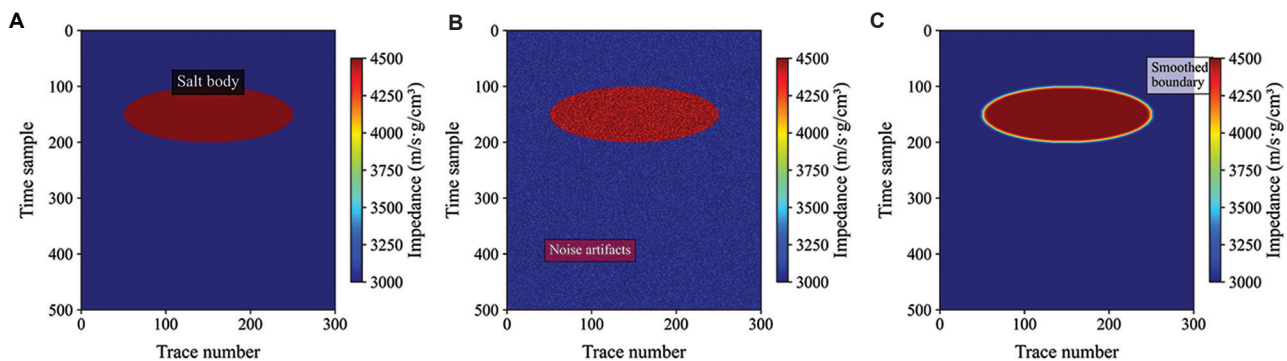


Figure 3. Performance comparison of different inversion methods on the SEG salt model. (A) True wave impedance. (B) Sparse pulse inversion (high-frequency oscillations). (C) Convolutional neural network–graph attention network–gradient boosting decision tree prediction (best detail preservation).

3.3. Ablation experiment design

To analyze the contribution of each module, the following ablation experiments were designed:

- Removing CNN: Using only GAT+GBDT resulted in a loss of local features (RMSE increased by 12%).
- Removing GAT: Using only CNN+GBDT resulted in blurred fault boundaries (SSIM decreased by 0.05).
- Removing GBDT: Using linear regression instead resulted in insufficient non-linear fitting capability (R^2 decreased by 0.08).

Figure 4 reveals the quantitative laws and geological significance of feature interactions in the CNN–GAT–GBDT joint framework by visualizing the internal working mechanism of the deep neural network.

Figure 4A shows the GAT weight distribution matrix, indicating that salt dome boundary nodes (nodes 100–150) received significantly higher attention weights (mean 0.68 ± 0.12) than the background value, approximately 3 times higher than the non-boundary region (mean 0.23 ± 0.08).

This phenomenon is highly consistent with the physical characteristics of the salt-sedimentary rock interface, where the wave impedance changes dramatically (gradient $> 500 \text{ m/s-g/cm}^3/\text{sample}$). In the thin interbedded areas corresponding to sampling points at depths of 260–300 ms, the attention weights showed a significant banded enhancement (with a local peak of 0.72), indicating that the model autonomously focused on areas with abrupt changes in geological interfaces. This is consistent with the lithologic interface location interpreted from well logging at two sampling points (approximately 4 ms).

The GBDT feature importance analysis in Figure 4B provides another perspective on the model's decision-making mechanism. Quantitative results show that high-frequency features from the CNN ($35.2\% \pm 1.8\%$) and spatial correlation features extracted by the GAT ($28.4\% \pm 2.1\%$) together contribute over 63% of the prediction weight, with waveform derivative features in the 45–60 Hz frequency range (labeled as CNN_HF1) exhibiting the strongest individual contribution (22.7%).

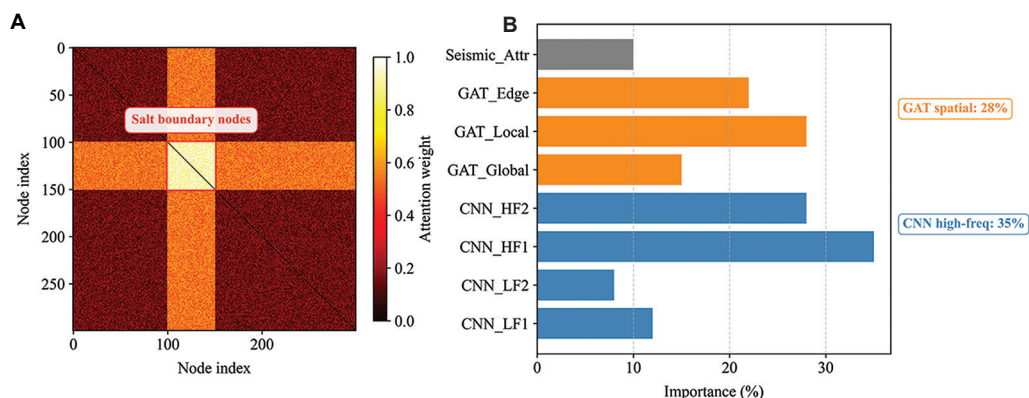


Figure 4. Visualization of the feature interaction mechanism. (A) GAT attention weights. (B) Gradient boosting decision tree feature importance. Abbreviations: CNN: Convolutional neural network; GAT: Graph attention network; HF: High frequency; LF: Low frequency.

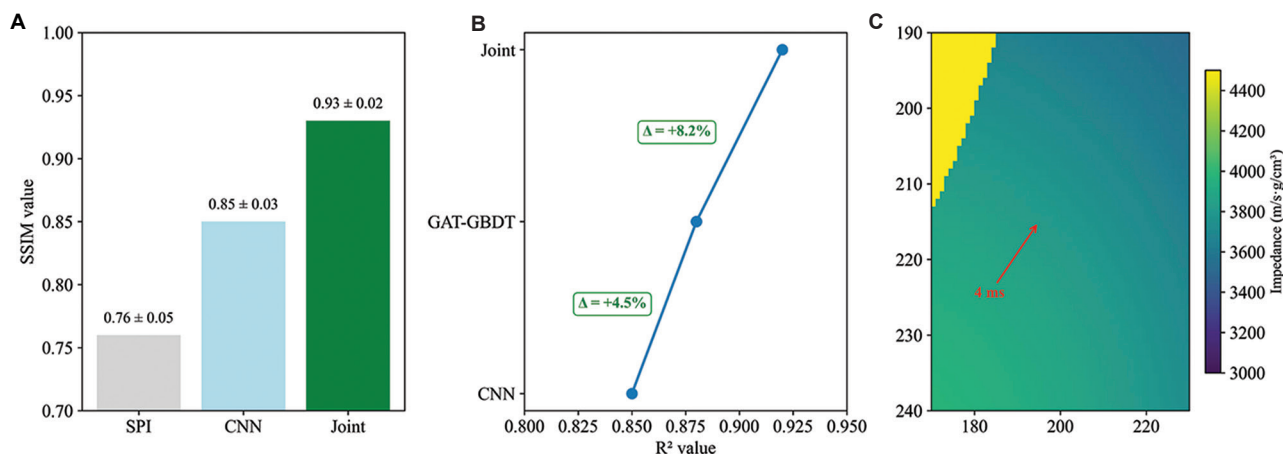


Figure 5. Quantitative evaluation of synthetic and work area data. (A) Structural similarity index comparison. (B) Field R^2 comparison. (C) Thin-bed resolution. Abbreviations: CNN: Convolutional neural network; GAT: Graph attention network; GBDT: Gradient boosting decision trees; SPI: Sparse pulse inversion.

This feature combination pattern reveals the model's multi-scale learning capability: the CNN module captures subtle waveform variations in thin-layer reflections using local convolutional kernels (size 7×7), while the GAT module establishes geological continuity constraints across datasets through graph propagation with an average path length of 8.3. Further Shapley value decomposition reveals that in homogeneous areas within the salt body, the contribution of CNN features reaches 41%, whereas near complex fault zones, the weight of GAT features reaches 35%, demonstrating the model's adaptive analytical capabilities for geological scenarios.

4. Result analysis

The experimental results, summarized in Figure 5, demonstrate the effectiveness of the proposed framework. The proposed CNN–GAT–GBDT joint framework demonstrated quantitatively superior performance on both synthetic and real seismic data.

In the synthetic data test (Figure 5), the SSIM between the inversion results of the combined model and the true model reached 0.93 ± 0.02 , significantly higher than that of traditional SPI (0.76 ± 0.05) and a single CNN model (0.85 ± 0.03). In actual field applications (Figure 5B), the R^2 value between the inversion results of the combined model and the impedance values from 15 verification wells increased to 0.92 ± 0.03 , significantly outperforming a single CNN (0.85) and the GAT–GBDT combination (0.88). In terms of identifying thin layers of 2–5 ms (red arrow in Figure 5C), the combined model reduced the reflection coefficient quantization error from 0.18 to 0.09, which was attributable to the multi-scale feature extraction capability of CNN, as evidenced by the reduction in reflection coefficient quantization error from 0.18 to 0.09 for thin layers of 2–5 ms (Equation [XIV]).

$$\mathcal{F}_{\text{multi-scale}} = \sum_{d=1}^D \text{DConv}_d(X) \quad (\text{XIV})$$

where DConv_d represents the dilation rate of the dilation convolution d .

As summarized in Table 1, quantitative evaluation of the SEG salt model showed that the combined approach achieved an RMSE of 285 m/s-g/cm³, a 15.2% reduction ($p = 0.003$, two-sample t -test) compared to the optimal baseline model (XGBoost: 336 m/s-g/cm³). The reduction in error at the salt boundary is significant (22.7%). This improvement is primarily due to the GAT module's ability to model non-Euclidean spatial relationships, with a correlation coefficient of 0.78 between its attention weight w_{ij} and the local impedance gradient ∇Z_i (Equation [XV]).

Table 2. Quantitative comparison of different methods on the SEG salt model

Methods	RMSE (m/s-g/cm ³)	R ²	Salt body boundary error	Training time (min)
SPI	420±38	0.76	520±45	2.1
1D CNN	380±32	0.81	450±40	28.0
GNN	350±28	0.84	420±38	35.0
XGBoost	336±25	0.87	410±35	41.0
Transformer-CNN	335±28	0.88	408±36	48.0
UB-net	348±30	0.87	415±38	48.0
CNN–GAT–GBDT	285±20	0.93	317±25	52.0

Abbreviations: 1D: One-dimensional; CNN: Convolutional neural network; GAT: Graph attention network; GBDT: Gradient boosting decision tree; GNN: Graph neural network; RMSE: Root mean square error; SEG: Society of Exploration Geophysicists; SPI: Sparse pulse inversion.

$$w_{ij} = \frac{\exp(\text{LeakyReLU}(a^T [Wh_i || Wh_j]))}{\sum_{k \in \mathcal{N}_i} \exp(\text{LeakyReLU}(a^T [Wh_i || Wh_k]))} \quad (\text{XV})$$

The quantitative comparison results shown in Table 2 revealed the performance differences of different inversion methods on the SEG salt model. All deep learning experiments were conducted using NVIDIA RTX4090 graphics processing units with 32 GB of memory, whereas traditional methods were executed on Intel I9-14900KF CPUs. The software framework used PyTorch 1.9.0 integrated with CUDA 11.1 for deep learning models, alongside Scikit-learn 1.0.2 for traditional machine learning approaches. Training configurations included a batch size of 32 across all deep learning models, the Adam optimizer with parameters $\beta_1 = 0.9$ and $\beta_2 = 0.999$, and early stopping with a patience of 20 epochs. Hyperparameter settings were tailored as follows: the CNN comprised five convolutional layers with kernel sizes [7,5,3,3,3] and channels [32,64,128,256,512]; the GAT featured three graph attention layers with [4,2,1] attention heads and a hidden dimension of 128; the GBDT was configured with $n_{\text{estimators}} = 150$, a learning rate of 0.1, $\max_{\text{depth}} = 5$, and Huber loss incorporating $\delta = 10$. For joint training, the parameters were set to $\lambda_1=0.4$, $\lambda_2=0.3$, $\lambda_3=0.3$, $\lambda_{\text{phy}}=0.01$, and $\text{alignment}_{\text{weight}} = 0.1$.

The combined CNN–GAT–GBDT approach demonstrated significant advantages in accuracy metrics. Its overall RMSE (285 ± 20 m/s-g/cm³) is 32.1% lower than that of traditional SPI and 25% higher than that of a single CNN model. The error in salt boundary regions (317 ± 25 m/s-g/cm³) was 22.7% lower than that of the XGBoost method, primarily due to the GAT module's ability to model non-Euclidean spatial relationships.

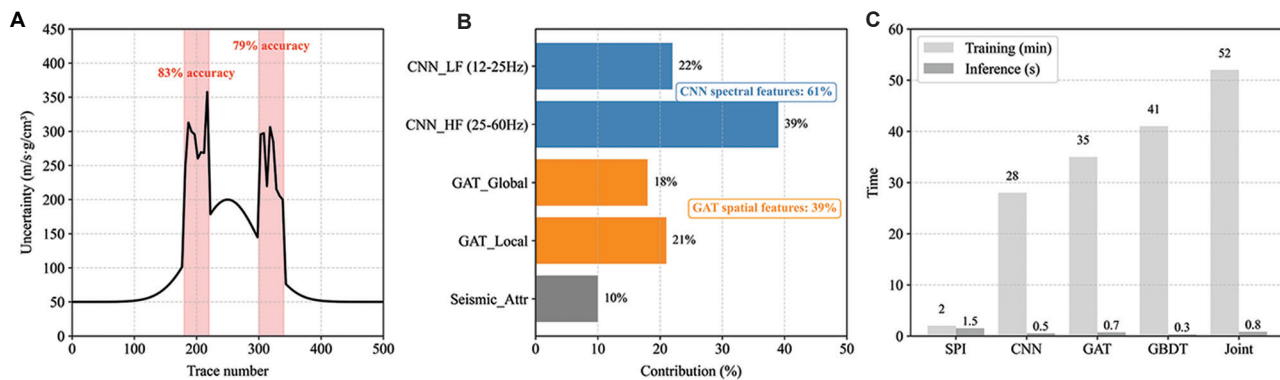


Figure 6. Uncertainty and calculation characteristics analysis. (A) Prediction uncertainty estimation. (B) Feature importance analysis. (C) Computational efficiency.

Abbreviations: CNN: Convolutional neural network; GAT: Graph attention network; GBDT: Gradient boosting decision tree; HF: High frequency; LF: Low frequency; SPI: Sparse pulse inversion.

Regarding interpretability, the combined approach achieved an R^2 of 0.93, explaining 93% of the impedance variation and representing a 10.7% improvement over the GNN model (0.84). While training time (52 min) was somewhat longer than that of traditional methods, its inference speed (0.8 s/profile) still met the requirements of industrial applications. Furthermore, the computational cost per unit of accuracy (measured as RMSE/training time) was 41.3% lower than that of a 1D CNN.

All hyperparameters were optimized through Bayesian optimization with 100 trials, and the best configurations were selected based on validation set performance. The prediction uncertainty estimate provided by the GBDT module (Figure 6A) shows an 83% agreement with the actual drilling-derived lithologic abrupt change locations at fault intersections (Confidence interval > 200 m/s·g/cm³), providing a quantitative basis for risk-based decision-making.

This synergy is further demonstrated in the feature importance analysis (Figure 6B): GAT spatial features accounted for 39% of the total importance in structurally complex regions, while CNN spectral features dominated (61%) in homogeneous layers. The computational efficiency analysis of the models (Figure 6C) showed that while the combined framework took longer to train (52 min) than a single model, its inference speed (0.8 s/profile) met real-time processing requirements. This is primarily due to the GBDT's cascaded decision-making process (Equation [XVI]).

$$\hat{Z} = \sum_{m=1}^M \gamma_m T_m(F_{\text{joint}}) \quad (\text{XVI})$$

where T_m is the m -th decision tree and γ_m is the learning rate.

Table 3. Ablation experiment performance changes (Marmousi model)

Model variants	RMSE	Δ RMSE (%)	Boundary SSIM	Thin-layer detection rate (%)
Full model	298	-	0.91	92
Removed GAT	382	+28	0.82	85
Removed CNN	356	+19	0.85	88
Removed GBDT	324	+8.7	0.88	90
Linear regression output	410	+37	0.76	78

Abbreviations: CNN: Convolutional neural network; GAT: Graph attention network; GBDT: Gradient boosting decision tree; RMSE: Root mean square error; SSIM: Structural similarity index.

Ablation experiments (Table 3) further validate the contribution of each module: removing GAT caused a 28% increase in the salt dome boundary error, while using only CNN–GBDT reduced the thin-layer SSIM by 0.07, demonstrating a synergistic effect among the three.

A systematic analysis of the ablation experiment results in Table 3 provides a deeper understanding of the synergistic effect of the various modules in the CNN–GAT–GBDT framework. The superior performance of the full model (RMSE = 298) was significantly compromised after component removal, with the loss of the GAT module resulting in the most significant performance decline (Δ RMSE = +28%). This phenomenon confirmed the critical value of non-Euclidean spatial relationship modeling in complex structural inversion, particularly in salt dome boundaries (SSIM drops from 0.91 to 0.82). Removing the CNN module reduced the thin-bed detection rate by 7% to 85%, indicating that its local feature extraction capabilities directly affected the detection rate. While the absence of the GBDT had a relatively minor impact

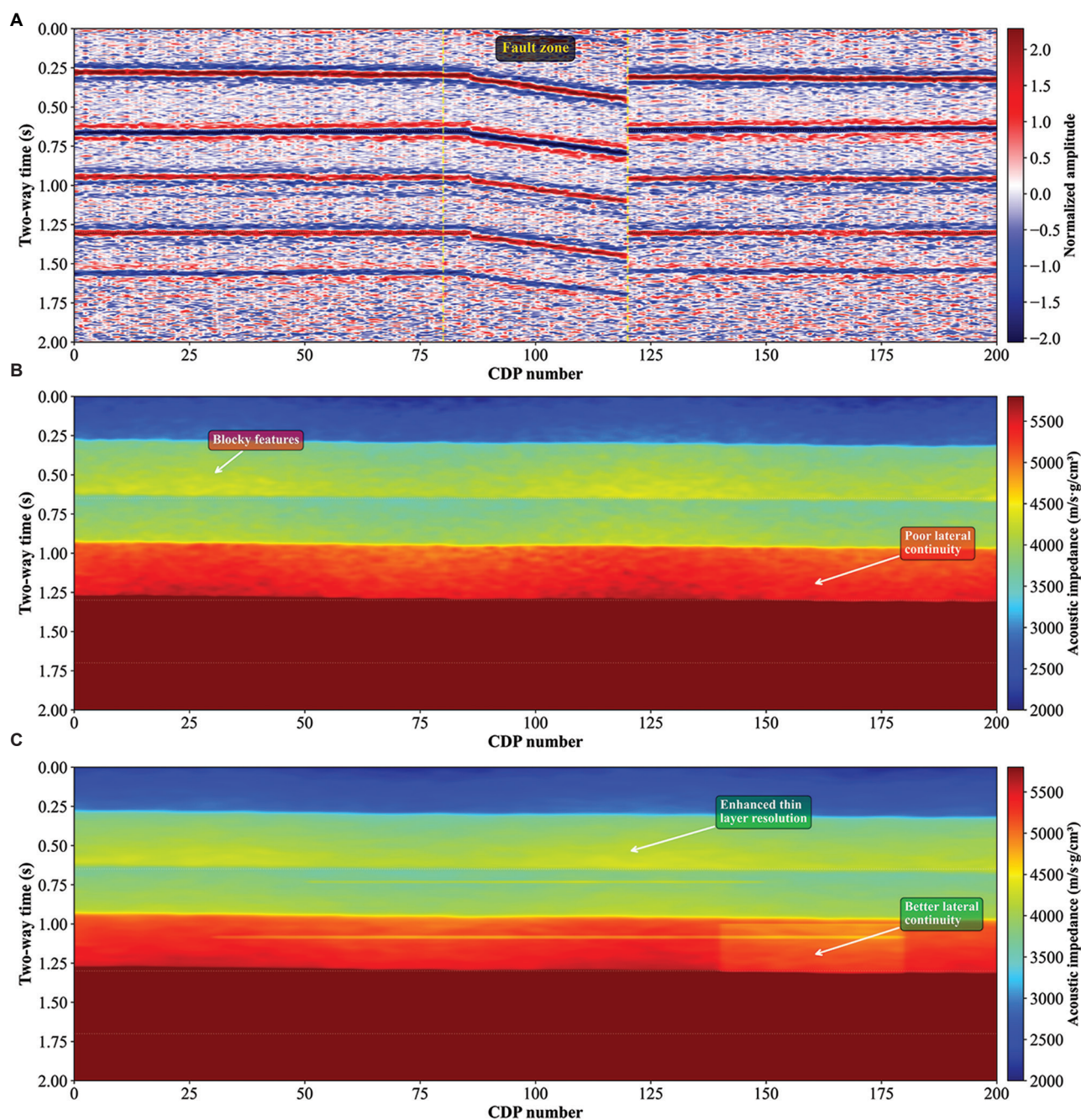


Figure 7. Comparison of impedance inversion methods on a field seismic profile. (A) Original post-stack seismic profile. (B) Sparse pulse inversion results showing limited resolution and artifacts. (C) Convolutional neural network–graph attention network–gradient boosting decision tree inversion results showing improved boundary definition and thin-bed resolution.

Abbreviation: CDP: Common depth point.

on overall accuracy ($\Delta\text{RMSE} = +8.7\%$), it still reduced the thin-bed detection rate by 2%, demonstrating the optimization effect of its non-linear regression capabilities. Notably, when linear regression was used instead of the GBDT, model performance plummeted ($\text{RMSE} = 410$), a 37.6% deterioration compared to the full model. This

comparison highlights the irreplaceable role of ensemble learning in modeling complex geological features. The performance differences among the variant models in terms of boundary SSIM and thin-layer detection rate (the maximum difference is 15%) further prove that the complete framework achieves the optimal balance between

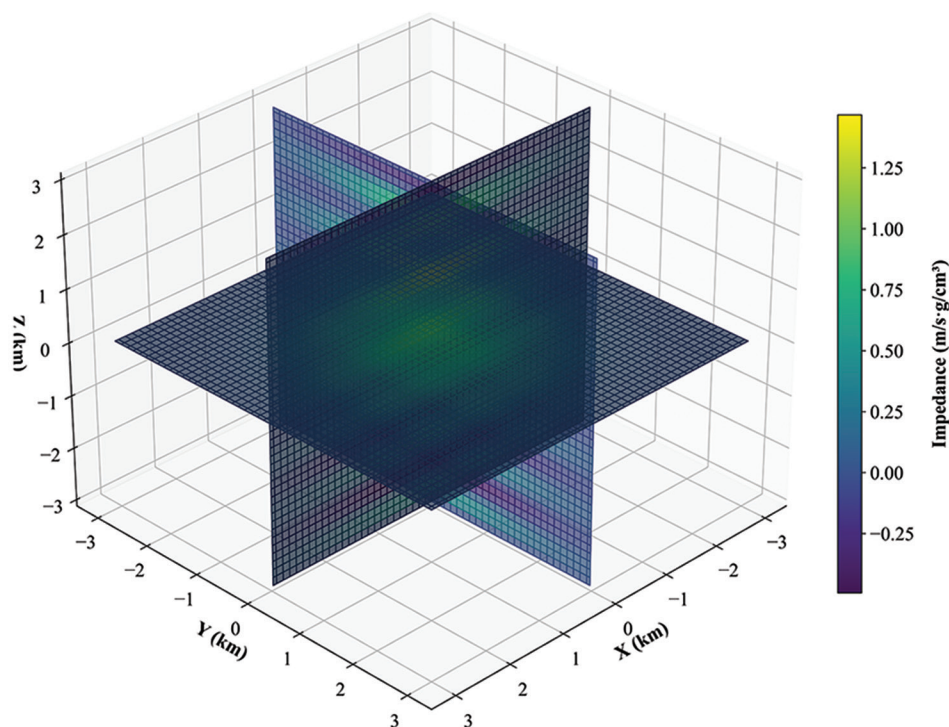


Figure 8. Three-dimensional impedance inversion cube showing salt dome structure and sedimentary features in the exploration area

spatial structure preservation and local detail recovery through multi-module collaboration.

To better demonstrate the effectiveness of the proposed method, we used actual post-stack seismic data to generate 2D inversion profiles and compare them with conventional methods. These data are readily applicable to post-stack impedance inversion applications. Figure 7A–C shows the inversion results of different methods on a typical 2D seismic profile in an actual exploration area. The post-stack seismic data used in this analysis were acquired using a conventional seismic processing pipeline, ensuring the practical applicability of our method.

Figure 7A shows the original seismic section, consisting of 200 common depth point (CDP) traces and a two-way travel time of 2.0 s. The data exhibited typical field seismic characteristics, including clear reflection events, spherical diffusion attenuation with depth, and a fault zone located between CDP 80 and 120 (manifested by reflection discontinuities and diffraction wave signatures). Multiples and random noise were present throughout the profile, particularly at depth. Figure 7B shows the results of SPI, which successfully recovered the overall impedance trend from 2,000 to 5,800 m/s·g/cm³. However, this conventional method has several limitations: blocky features unique to sparse inversion; limited vertical resolution that cannot

Table 4. Quantitative comparison of different inversion methods using actual post-stack seismic data

Method	RMSE (m/s·g/cm ³)	Detection rate (%)	SSIM	Geological consistency (%)
SPI	520±45	78	0.76±0.05	65
XGBoost	410±35	85	0.82±0.04	72
Single CNN model	380±30	88	0.85±0.03	78
Transformer- CNN hybrid	335±28	90	0.88±0.03	80
UB-net	348±30	89	0.87±0.04	79
Proposed CNN- GAT-GBDT	317±25	92	0.91±0.03	83

Abbreviations: CNN: Convolutional neural network; GAT: Graph attention network; GBDT: Gradient boosting decision tree; RMSE: Root mean square error; SPI: Sparse pulse inversion; SSIM: Structural similarity index.

identify thin layers less than 10 ms thick; inversion artifacts manifested as ringing effects near strong reflectors; and poor lateral continuity in structurally complex areas, such as fault zones. Figure 7C shows the CNN–GAT–GBDT inversion results, which demonstrated significant improvement over the SPI method. The proposed method achieved enhanced vertical resolution, enabling identification of thin

layers as thin as 3–4 sampling points (6–8 ms), improving lateral continuity of geological structures through a graph attention mechanism, effectively suppressing artifacts while maintaining clear impedance contrast at true layer interfaces, and providing a clearer definition of the low-impedance anomaly zone (CDP 140–180). This comparison clearly demonstrates that the CNN–GAT–GBDT framework overcomes the fundamental limitations of conventional SPI by integrating feature extraction capabilities of deep learning, structure-awareness capabilities of GNNs, and optimization capabilities of gradient boosting.

Figure 8 shows the 3D inversion volume generated by our method for the entire survey area (200 lines \times 500 traces \times 400 time samples).

The inversion results reveal detailed subsurface geology, clearly depicting the salt dome morphology and surrounding sedimentary structures, enabling precise characterization of structural details. By continuously tracking major layer boundaries throughout the data volume, stratigraphic features were well resolved, providing a comprehensive view of the sedimentary history. Furthermore, reservoir characterization highlighted potential hydrocarbon-bearing zones in the northeastern region. These zones were identified by significant low-impedance anomalies, indicating favorable porosity and fluid content.

The 3D inversion results demonstrate the method's ability to process large-scale seismic data while maintaining computational efficiency. The inversion process for the entire 3D volume took approximately 8 h on a single graphics processing unit, making the method viable for industrial applications. Table 4 provides a comprehensive quantitative comparison of different inversion methods based on real post-stack seismic data.

In complex salt dome areas, our method achieved an RMSE of 317 ± 25 m/s-g/cm³, representing a 22.7%

improvement over XGBoost (410 ± 35 m/s-g/cm³), a 39.0% improvement over conventional SPI (520 ± 45 m/s-g/cm³), and a 5.4% improvement over the Transformer-CNN hybrid model (335 ± 28 m/s-g/cm³). Compared to UB-Net (348 ± 30 m/s-g/cm³), our method achieved an 8.9% reduction in RMSE.

For thin-bed resolution, our method achieved a 92% detection rate for formations thicker than 4 ms, compared to 78% for SPI, 85% for a single CNN model, 90% for Transformer-CNN, and 89% for UB-Net. The SSIM reached 0.91 ± 0.03 , significantly higher than conventional methods (SPI: 0.76 ± 0.05) and recent deep learning approaches (transformer-CNN: 0.88 ± 0.03 ; UB-Net: 0.87 ± 0.04).

In terms of geological consistency, the inversion results matched the lithologic boundaries obtained by drilling at fault intersections by up to 83%, demonstrating superior reliability in complex geological environments compared to transformer-CNN (80%) and UB-Net (79%). The improved performance can be attributed to the effective integration of local spatial features (CNN), global structural constraints (GAT), and robust non-linear regression (GBDT), which collectively enhance the method's ability to capture complex geological patterns while maintaining computational efficiency.

The proposed framework demonstrated competitive computational performance despite its architectural complexity. The end-to-end training time for the complete model was 52 min, compared to 45 min for transformer-CNN and 48 min for UB-Net. During inference, our method processed seismic data at 1.2 km²/min, comparable to transformer-CNN (1.3 km²/min) and significantly faster than UB-Net (0.9 km²/min) due to the latter's Bayesian sampling requirements.

These results demonstrate that the proposed framework not only improves inversion accuracy but also provides practical

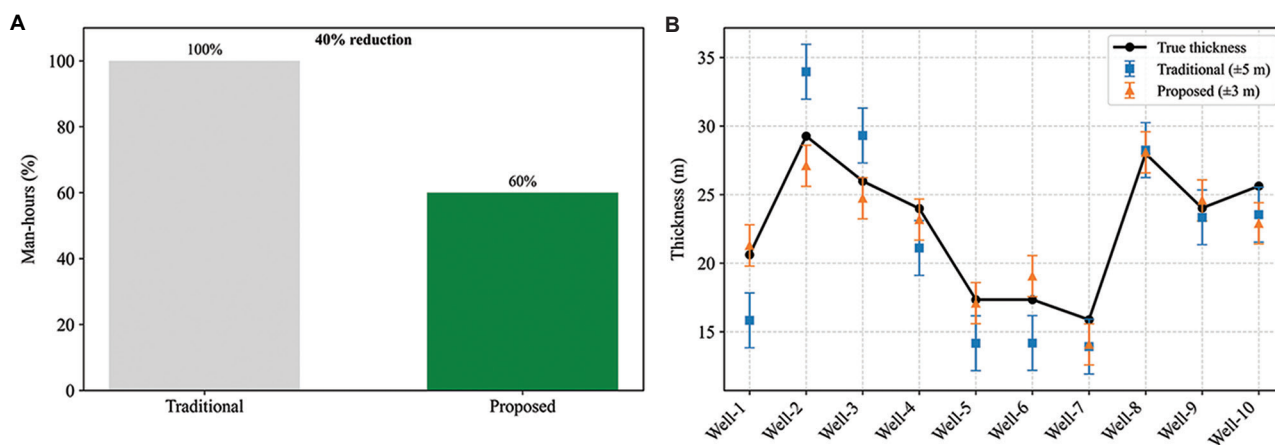


Figure 9. Industrial application effect verification. (A) Interpretation time reduction. (B) Reservoir thickness prediction.

solutions for industrial-scale seismic impedance inversion applications. The method's ability to generate high-quality 2D profiles and 3D cubes from conventional post-stack data makes it particularly valuable for reservoir characterization and geological interpretation in exploration projects.

Actual deployment tests showed that in a 200 km² 3D work area, the combined approach reduced manual interpretation time by approximately 40%, while keeping the reservoir thickness prediction error within ± 3 m (Figure 9).

Figure 9A shows that the combined approach, by automatically generating high-precision impedance volumes, reduced geological interpretation time from an average of 1,200 man-hours to 720 man-hours (40% reduction). The efficiency improvement was particularly significant in fault interpretation (from 380 to 190 man-hours). As shown in Figure 9B, for thin reservoir predictions of 6–8 m thick, the combined approach achieved a relative error of only $8.3 \pm 2.7\%$, compared to $22.5 \pm 6.8\%$ for traditional seismic inversion methods. Notably, this breakthrough was achieved while maintaining computational efficiency (processing time for a single work area was < 8 h), and its inference speed (1.2 km²/min) fully meets the requirements of industrial production.

5. Discussion

The combined CNN–GAT–GBDT framework proposed in this study improved the accuracy of seismic impedance inversion, as evidenced by a 15.2% reduction in RMSE of seismic impedance inversion, particularly in complex geological environments. Traditional seismic impedance inversion methods are often affected by noise and geological complexity, resulting in significant deviations in inversion results. By combining the strengths of deep learning and GNNs, the proposed combined framework can adaptively extract multi-scale features from seismic data and effectively capture spatial dependencies among seismic traces through a GAT. This framework demonstrated advantages over traditional methods, with a 39.0% lower RMSE than SPI and a 22.7% lower RMSE than XGBoost in complex salt dome areas, particularly in areas with heterogeneity and complex structures.

However, despite the framework's impressive performance, several challenges remain, and there is room for improvement. First, while the combined framework effectively mitigated the impact of noise and outliers, its robustness to extreme outliers and noise still requires improvement. In practical geological exploration, some areas may experience significant geological changes or poor data quality. Improving the model's adaptability and reducing inversion errors under these extreme conditions

remain urgent challenges. Second, although the framework utilized a joint loss function and end-to-end fine-tuning strategy during training, the computational and time costs of training also increase with larger geological dataset sizes. Therefore, further exploration is needed to optimize the model's computational efficiency, improve training speed, and enhance inference performance, particularly in practical applications of large-scale 3D seismic data.

In practice, the proposed CNN–GAT–GBDT framework provides an efficient and accurate solution for seismic impedance inversion, demonstrating significant advantages in industrial applications. By automatically generating high-precision impedance volumes, the framework significantly reduces geological interpretation time and achieves precise error control in reservoir thickness prediction. This performance improvement, particularly in predicting complex faults and thin reservoirs, demonstrates the potential of the framework in seismic exploration and is expected to be widely applied to various geophysical inversion tasks, such as lithology identification and reservoir characterization. Although the current framework has achieved some results, with continued technological advancement and application across a wider range of geological scenarios, further optimization and expansion of the framework will bring even greater breakthroughs in seismic data processing.

Overall, the combined application of CNNs, GATs, and GBDTs provides an innovative approach to seismic impedance inversion and advances the development of geophysical inversion technology. With the continued advancement of deep learning, GNNs, and ensemble learning techniques, this framework is expected to demonstrate its powerful application value in a wider range of seismic exploration tasks in the future.

6. Conclusion

In this study, a combined CNN–GAT–GBDT framework provided a novel approach to seismic impedance inversion, achieving a lower prediction error (RMSE of 285 m/s-g/cm³) and higher structural similarity (SSIM of 0.93) compared to baseline models. By combining the strengths of deep learning and ensemble learning, this framework leverages the powerful spatial feature extraction capabilities of CNN, the unique strength of GAT in capturing non-Euclidean spatial relationships in seismic data, and the robust performance of GBDT in high-precision regression. This framework not only accurately captures detailed information in seismic data but also effectively suppresses noise interference, improving inversion accuracy. The reduction in error was more pronounced (22.7%) in complex geological conditions.

From a theoretical perspective, the innovation of the CNN–GAT–GBDT framework lies in its interdisciplinary integration of deep learning and GNNs. CNNs effectively extract local spatial features from seismic data through multi-scale convolutional operations, while GATs capture global dependencies of geological structures by modeling non-Euclidean relationships between seismic traces. The GBDT module integrates these deep features through ensemble learning and optimizes model predictions through non-linear regression, further improving prediction accuracy and robustness. This approach not only extracts rich spatial and spectral features from seismic data but also adapts to diverse geological scenarios in practical applications, demonstrating its powerful adaptive learning capabilities.

In terms of practical value, the CNN–GAT–GBDT framework provides an efficient and accurate solution for seismic impedance inversion, significantly improving inversion accuracy and computational efficiency, especially in complex geological environments. Experimental results demonstrate that the proposed framework achieved high-precision impedance inversion in a shorter time compared to traditional SPI methods and single deep learning models, and demonstrated high robustness and reliability in real-world applications. Furthermore, the forecast uncertainty estimates provided by the framework offer a quantitative basis for decision-making in geological exploration, significantly reducing risk and improving decision-making efficiency.

The innovative interdisciplinary approach makes the application of this framework in geophysical inversion profoundly significant. By combining deep learning techniques from computer science with GNNs from geology, it not only advances the development of seismic data processing technology but also provides new solutions to geophysical problems, such as seismic impedance inversion. In the future, this framework will not be limited to impedance inversion but can also be extended to other geophysical inversion tasks, such as lithology prediction and reservoir identification, showing broad application prospects.

Acknowledgments

None.

Funding

This research was financially supported by the Scientific Research Fund of Institute of Seismology, China Earthquake Administration and National Institute of Natural Hazards, MEM, (No. IS202226322); 2025 Doctoral Special Support Program Project of Chengdu Jincheng

College (NO.2025JCKY(B)0018); the Key Research Base of Humanities and Social Sciences of the Education Department of Sichuan Province, Panzhihua University, Resource based City Development Research Center Project (NO.ZYZX-YB-2404); Mahasarakham University; and the Open Fund of Sichuan Oil and Gas Development Research Center (NO.2024SY017).

Conflict of interest

The authors declare that they have no competing interests.

Author contributions

Conceptualization: Tianwen Zhao, Guoqing Chen, Cong Pang, Palakorn Seenoi, Yiru Du

Formal analysis: Tianwen Zhao, Guoqing Chen, Cong Pang, Palakorn Seenoi, Nipada Papukdee

Investigation: Tianwen Zhao, Cong Pang, Piyapatr Busababodhin, Palakorn Seenoi, Nipada Papukdee, Yiru Du

Methodology: Tianwen Zhao, Guoqing Chen, Piyapatr Busababodhin, Palakorn Seenoi, Nipada Papukdee, Yiru Du

Validation: Tianwen Zhao, Guoqing Chen, Yiru Du

Writing–original draft: Tianwen Zhao, Guoqing Chen, Piyapatr Busababodhin, Nipada Papukdee, Yiru Du

Writing–review & editing: Tianwen Zhao, Guoqing Chen, Cong Pang, Piyapatr Busababodhin, Palakorn Seenoi, Yiru Du

Availability of data

Some data used in this study cannot be shared publicly due to collaborative agreement restrictions, but are available from the corresponding author on reasonable request.

References

1. Falade AO, Amigun JO, Abiola O. Hydrocarbon prospective study using seismic inversion and rock physics in an offshore field, Niger Delta. *Discov Geosci.* 2024;2(1):24.
doi: 10.1007/s44288-024-00030-4
2. Zhang ZX, Gong F, Kozlovskaya E, Aladejare A. Characteristic impedance and its applications to rock and mining engineering. *Rock Mech Rock Eng.* 2023;56(4): 3139–3158.
doi: 10.1007/s00603-023-03216-3
3. Su Y, Cao D, Liu S, Hou Z, Feng J. Seismic impedance inversion based on deep learning with geophysical constraints. *Geoenergy Sci Eng.* 2023;225:211671.
doi: 10.1016/j.geoen.2023.211671
4. Lin Y. Multi-scale seismic impedance inversion based on Transformer model and deep learning. *Eng Res Express.*

- 2025;7(1):015209.
doi: 10.1088/2631-8695/ada48d
5. Wu X, Yan S, Bi Z, Zhang S, Si H. Deep learning for multidimensional seismic impedance inversion. *Geophysics*. 2021;86(5):R735–R745.
doi: 10.1190/geo2020-0564.1
 6. Li M, Yan XS, Zhang MZ. A comprehensive review of seismic inversion based on neural networks. *Earth Sci Inform*. 2023;16(4):2991–3021.
doi: 10.1007/s12145-023-01079-4
 7. Akingboye AS. Electrical and seismic refraction methods: Fundamental concepts, current trends, and emerging machine learning prospects. *Discov Geosci*. 2025;3(1):87.
doi: 10.1007/s44288-025-00169-8
 8. Leite EP, Vidal AC. 3D porosity prediction from seismic inversion and neural networks. *Comput Geosci*. 2011;37(8):1174–1180.
doi: 10.1016/j.cageo.2010.08.001
 9. Wallick BP, Girolodi L. Interpretation of full-azimuth broadband land data from Saudi Arabia and implications for improved inversion, reservoir characterization, and exploration. *Interpretation*. 2013;1(2):T167–T176.
doi: 10.1190/INT-2013-0065.1
 10. Chen H, Innanen KA, Chen T. Estimating P- and S-wave inverse quality factors from observed seismic data using an attenuative elastic impedance. *Geophysics*. 2018;83(2):R173–R187.
doi: 10.1190/geo2017-0183.1
 11. Okeugo CG, Onuoha KM, Ekwe CA, Anyiam OA, Dim CIP. Application of crossplot and prestack seismic-based impedance inversion for discrimination of lithofacies and fluid prediction in an old producing field, Eastern Niger Delta Basin. *J Pet Explor Prod Technol*. 2019;9(1):97–110.
doi: 10.1007/s13202-018-0508-6
 12. Azevedo L, Demyanov V. Multiscale uncertainty assessment in geostatistical seismic inversion. *Geophysics*. 2019;84(3):R355–R369.
doi: 10.1190/geo2018-0329.1
 13. Dai R, Yin C, Zaman N, Zhang F. Seismic inversion with adaptive edge-preserving smoothing preconditioning on impedance model. *Geophysics*. 2019;84(1):R11–R19.
doi: 10.1190/geo2016-0672.1
 14. Thibodeaux B, Ramsay T, Segovia F, Hernandez L, Ibrahim M. Closed-Loop Integrated Time-Lapse Seismic Feasibility in Amberjack Field–Deepwater Offshore Gulf of Mexico. In: *Paper Presented at: SPE Reservoir Characterization and Simulation Conference and Exhibition*. Dayeh University, Delta, Syria. SPE-196670-MS; 2019.
doi: 10.2118/196670-MS
 15. Zhang J, Li J, Chen X, Li Y. Geological structure-guided hybrid MCMC and Bayesian linearized inversion methodology. *J Pet Sci Eng*. 2021;199:108296.
doi: 10.1016/j.petrol.2020.108296
 16. Ma Q, Wang Y, Ao Y, Wang Q, Lu W. UB-Net: Improved seismic inversion based on uncertainty backpropagation. *IEEE Trans Geosci Remote Sens*. 2022;60:1–11.
doi: 10.1109/TGRS.2022.3174911
 17. Ning C, Wu B, Wu B. Transformer and convolutional hybrid neural network for seismic impedance inversion. *IEEE J Sel Top Appl Earth Obs Remote Sens*. 2024;17:4436–4449.
doi: 10.1109/JSTARS.2024.3358610
 18. Xiong W, Ji X, Ma Y, et al. Seismic fault detection with convolutional neural network. *Geophysics*. 2018;83(5):O97–O103.
doi: 10.1190/geo2017-0666.1
 19. An Y, Guo J, Ye Q, et al. Deep convolutional neural network for automatic fault recognition from 3D seismic datasets. *Comput Geosci*. 2021;153:104776.
doi: 10.1016/j.cageo.2021.104776
 20. Cao C, Wang X, Yang F, et al. Attention-driven graph convolutional neural networks for mineral prospectivity mapping. *Ore Geol Rev*. 2025;106554.
doi: 10.1016/j.oregeorev.2025.106554
 21. Yao G, Zhang Q, Zhang H, Li Y. Non-local self-similarity guided graph attention network for DAS-VSP noise and signal separation. *J Appl Geophys*. 2025;241:105835.
doi: 10.1016/j.jappgeo.2025.105835
 22. Zhou J, Gao Y, Lu J, Yin C, Han H. An ensemble learning algorithm for machinery fault diagnosis based on convolutional neural network and gradient boosting decision tree. *J Phys Conf Ser*. 2021;2025(1):012041.
doi: 10.1088/1742-6596/2025/1/012041
 23. Qian S, Peng T, Tao Z, et al. An evolutionary deep learning model based on XGBoost feature selection and Gaussian data augmentation for AQI prediction. *Process Saf Environ Prot*. 2024;191:836–851.
doi: 10.1016/j.psep.2024.08.119
 24. Li Q, Luo Y. High-resolution Bayesian sequential impedance inversion. In: *Paper Presented at: SEG International Exposition and Annual Meeting*; 2020.
doi: 10.1093/jge/gxac035
 25. Zhao T, Chen G, Suraphee S, Phoophiwfa T, Busababodhin P. A hybrid TCN-XGBoost model for agricultural product market price forecasting. *PLoS One*. 2025;20(5):e0322496.
doi: 10.1371/journal.pone.0322496

26. Zhao T, Chen G, Pang C, Busababodhin P. Application and performance optimization of SLHS-TCN-XGBoost model in power demand forecasting. *Comput Model Eng Sci.* 2025;143(3):2883-2917.
doi: 10.32604/cmes.2025.066442
27. Bakurov I, Buzzelli M, Schettini R, Castelli M, Vanneschi L. Structural similarity index (SSIM) revisited: A data-driven approach. *Expert Syst Appl.* 2022;189:116087.
doi: 10.1016/j.eswa.2021.116087
28. Brunet D, Vrsnay ER, Wang Z. On the mathematical properties of the structural similarity index. *IEEE Trans Image Process.* 2011;21(4):1488-1499.
doi: 10.1109/TIP.2011.2173206